ISPRS Journal of Photogrammetry and Remote Sensing 115 (2016) 90–102

Contents lists available at ScienceDirect

ISPRS Journal of Photogrammetry and Remote Sensing

journal homepage: www.elsevier.com/locate/isprsjprs

Review Article

# Time series analysis of InSAR data: Methods and trends

Batuhan Osmanoğlu [a,*], Filiz Sunar [b], Shimon Wdowinski [c], Enrique Cabral-Cano [d]

[a] USRA – NASA Goddard Space Flight Center, USA
[b] Istanbul Technical University, Istanbul, Turkey
[c] University of Miami – RSMAS, USA
[d] Departamento de Geomagnetismo y Exploración, Instituto de Geofísica, Universidad Nacional Autónoma de México, Ciudad Universitaria, México D.F. 04510, Mexico

ARTICLE INFO

*Article history:*
Received 31 May 2015
Received in revised form 7 October 2015
Accepted 7 October 2015
Available online 6 November 2015

*Keywords:*
InSAR
Multi-temporal InSAR
Persistent scatterer InSAR
Small baselines subset

ABSTRACT

Time series analysis of InSAR data has emerged as an important tool for monitoring and measuring the displacement of the Earth's surface. Changes in the Earth's surface can result from a wide range of phenomena such as earthquakes, volcanoes, landslides, variations in ground water levels, and changes in wetland water levels. Time series analysis is applied to interferometric phase measurements, which wrap around when the observed motion is larger than one-half of the radar wavelength. Thus, the spatio-temporal "unwrapping" of phase observations is necessary to obtain physically meaningful results. Several different algorithms have been developed for time series analysis of InSAR data to solve for this ambiguity. These algorithms may employ different models for time series analysis, but they all generate a first-order deformation rate, which can be compared to each other. However, there is no single algorithm that can provide optimal results in all cases. Since time series analyses of InSAR data are used in a variety of applications with different characteristics, each algorithm possesses inherently unique strengths and weaknesses. In this review article, following a brief overview of InSAR technology, we discuss several algorithms developed for time series analysis of InSAR data using an example set of results for measuring subsidence rates in Mexico City.



## 1. Introduction

Synthetic Aperture Radar (SAR) systems emit electromagnetic (EM) waves and collect the returned energy from a target in the antenna look direction. Many radar systems emit coherent radiation in the microwave portion of the spectrum, meaning that the EM radiation has a sinusoidal radiation pattern with amplitudes going through well-defined minima and maxima. Each wavelength (distance between two consecutive maxima or minima) corresponds to 360° or 2π radians. Wavelength defines the unit distance for SAR phase measurements.

SAR measurements have two observables: amplitude, and phase. The amplitude is the strength of the back-scattered EM wave and is related to the targets shape, orientation, and electrical properties. As the wave propagates in the air, the phase of the wave changes from $-\pi$ to $+\pi$ for every wavelength of distance traveled. SAR systems can measure the phase of the return signal very precisely, but the range, the total number of wavelengths, is difficult to measure directly. This is similar to having a very accurate analog watch, without the minute or hour hands. Even though this watch would be capable of measuring small variations differently, time frames over a minute ($360^0$ rotation of the second hand) would result in ambiguous measurements. InSAR phase measurements detect changes between two SAR acquisitions, which are generally referred to as master and slave acquisitions. Fig. 1 illustrates the basic phase observable for a typical InSAR measurement.

In a simplified scenario the phase return of a single point scatterer is given as (Hanssen, 2001):

$$\varphi = 2R_p 2\pi/\lambda + \varphi_{scat} \tag{1.1}$$

where

$\varphi$ is phase,
$R_p$ is range between radar and the point on the ground,
$\lambda$ is the radar wavelength and
$\varphi_{scat}$ denotes the scattering phase contribution and is related to the target's electrical properties.

InSAR measurements are especially sensitive to topography, ground motion, atmospheric conditions, spatial separation

* Corresponding author.
*E-mail addresses:* batuhan.osmanoglu@nasa.gov (B. Osmanoğlu), fsunar@itu.edu.tr (F. Sunar), swdowinski@rsmas.miami.edu (S. Wdowinski), ecabral@geofisica.unam.mx (E. Cabral-Cano).

http://dx.doi.org/10.1016/j.isprsjprs.2015.10.003
0924-2716/

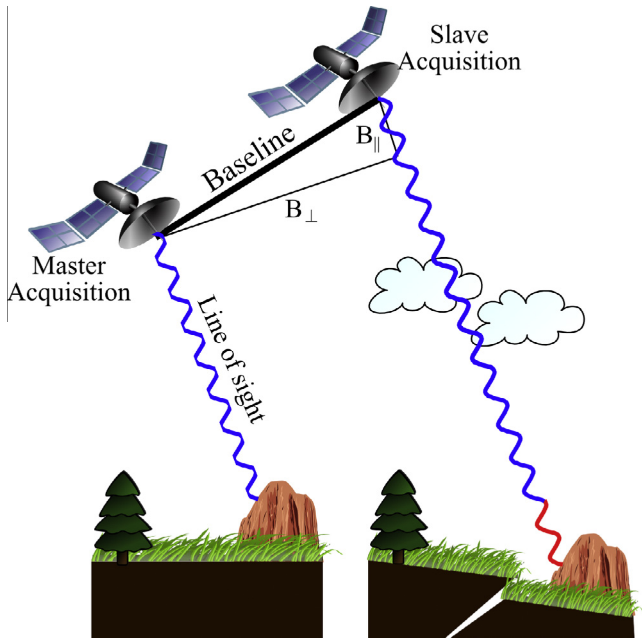


**Fig. 1.** Schematic illustration explaining the repeat pass interferometry. Initial (master) acquisition displays the line-of-sight and phase measurement. Using the position of the second acquisition (slave), perpendicular ($B_{\perp}$), parallel ($B_{\parallel}$) baseline vectors are formed. The sum of perpendicular and parallel baselines define total spatial baseline between master and slave. Red portion of the measured signal corresponds to the difference in phase measurements. (For interpretation of the references to color in this figure legend, the reader is referred to the web version of this article.)

between satellites, and the electrical properties of the ground as shown in Eq. (1.2) (Ferretti et al., 2001; Colesanti et al., 2003). InSAR phase signal is a lumped sum of changes in all these factors, and depending on the application some factors can be considered noise. For example, if generating a Digital Elevation Model (DEM) is the main goal, then deformation can be considered noise. In a similar way, the time series analysis methods have to remove the stable topographic phase contribution (DEM) to obtain the ground motion.

$$\Delta\varphi = \varphi_{flat} + \varphi_{topo} + \varphi_{orbit} + \varphi_{defo} + \varphi_{tropo} + \varphi_{iono} + \varphi_{scat} + \varphi_{noise} \tag{1.2}$$

where
- $\Delta\varphi$: interferometric phase (or phase change between SAR acquisitions),
- $\varphi_{flat}$: flat earth phase,
- $\varphi_{topo}$: topographic phase contribution,
- $\varphi_{orbit}$: the phase error induced by errors in orbit information,
- $\varphi_{defo}$: phase contribution related to ground deformation,
- $\varphi_{tropo}$: tropospheric phase contribution,
- $\varphi_{iono}$: ionospheric phase contribution,
- $\varphi_{scat}$: phase contribution related to the scatterer's electrical properties,
- $\varphi_{noise}$: the combined noise term.

Flat earth ($\varphi_{flat}$), topographic phase ($\varphi_{topo}$) and ground deformation ($\varphi_{defo}$) are all parts of the range difference equation between two passes, which is a function of the satellite orbits, and topography. The change in range is related to phase based on the equation (Bamler and Hartl, 1998):

$$\Delta\varphi_{flat,topo,defo} = 4\pi/\lambda \cdot \Delta R \tag{1.3}$$

where $\lambda$ denotes the radar wavelength, and $\Delta R$ indicates the range change between first and second passes of the satellite. The flat earth phase is due to the shape of the Earth, which can be calculated given the satellite orbits and the geodetic datum (i.e. WGS84). Most SAR imaging software focus the images with the assumption of a flat earth, hence the phase difference between flat and actual earth has to be considered. The flat earth phase is related to the parallel baseline as follows (DEOS, 2009):

$$\varphi_{flat} = 4\pi/\lambda \cdot B_{\parallel} \tag{1.4}$$

where the $B_{\parallel}$ is the parallel baseline for each pixel. Topographic phase is the phase component of the interferogram related to the topography above the reference ellipsoid and it is proportional to the perpendicular baseline as shown in Eq. (1.5) (Ferretti et al., 2007a):

$$\varphi_{topo} = 4\pi/\lambda \cdot /B_{\perp}/R\sin\theta \cdot \Delta z \tag{1.5}$$

where $\varphi_{topo}$ is topographic phase contribution, $B_{\perp}$ is perpendicular baseline, $R$ is range between target and satellite, $\theta$ is antenna look angle, and $\Delta z$ is topography above the reference ellipsoid. In Eqs. (1.4) and (1.5) the flat earth and topographic phase values are given relative to the baselines ($B_{\parallel}$ and $B_{\perp}$). Therefore any error in the orbit information will result in residual phase error, which is shown as $\varphi_{orbit}$. Deformation is also a part of the interferometric phase and is measured in the line-of-sight direction. Deformation is positive when the range between satellite and the ground is increasing, which maps subsidence as positive phase change. Given that deformation is denoted by $\Delta R_{defo}$ the interferometric phase due to deformation is given by (Ferretti et al., 2007a):

$$\Delta\varphi_{defo} = 4\pi/\lambda \cdot \Delta R_{defo} \tag{1.6}$$

Differences in atmospheric conditions during the acquisitions of master and slave images also contribute to the interferometric phase measurements. Tropospheric phase contribution results from the refractivity index of troposphere being slightly above that of free space, which has a refractivity of 1 (Zebker et al., 1997). Tropospheric phase delay can be separated into wet and dry components, and is generally contained within a phase cycle (Ferretti et al., 2007a).

$$\varphi_{tropo} = 4\pi/\lambda \cdot \Delta R_{tropo} \tag{1.7}$$

where $\Delta R_{tropo}$ indicates the range change due to atmospheric delay. The atmospheric phase contribution can be estimated using external measurements like the Envisat MERIS (Moisseev et al., 2005) and atmospheric models (Hanssen and Feijt, 1997; Zebker et al., 1997). Generally the tropospheric phase contribution is referred as the atmospheric phase screen (APS) for C-band (4–6 GHz) and higher frequency radars. However, for L-band (1–2 GHz) and lower frequency radars, changes in the ionospheric total electron content (TEC) can also affect the interferometric phase significantly. Changes in ionospheric conditions can also cause blurring in range and azimuth directions, introducing challenges for image coregistration, as well as reducing coherence due to Faraday rotation (Meyer and Nicoll, 2009; Wegmuller et al., 2006). 1 unit of TEC difference ($10^{16}$ m$^{-2}$) would result in a phase delay of 2 cycles at L-band, 0.5 cycles at C-band and 0.3 cycles at X-band given by the following formula (Wegmuller et al., 2006):

$$\varphi_{iono} = 1.69 \cdot 10^{-6} N\lambda \tag{1.8}$$

where $N$ is the number of electrons per unit area, and $\lambda$ is the wavelength.

The phase contribution due to changes in the scatterer's electrical properties are usually assumed negligible for topography and deformation observations. However, there are studies on estimating penetration depth, water equivalent of dry snow, and soil moisture (Guneriussen et al., 2002; Nolan and Fatland, 2003; Nolan et al., 2004) based on the changes in dielectric properties of the scatterer. It must be noted that the interferometric measurements can reflect changes in different phenomena. Therefore, certain assumptions are often made to analyze the results. In general, the larger signal dominates the interferogram and smaller signals like changes in penetration depth are often masked by bigger signals like ground deformation or topography. Study of smaller signals requires a good understanding of the larger contributors so that their effects can be minimized.

The interferometric phase noise term ($\varphi_{noise}$) can be linked to coherence and be broken into four different decorrelation terms (Zebker and Villasenor, 1992). The effect of different decorrelation terms is multiplicative and can be given as:

$$\gamma_{total} = \gamma_{spatial} + \gamma_{Doppler} + \gamma_{temporal} + \gamma_{thermal} \tag{1.9}$$

where $\gamma_{total}$ is the total correlation (interferometric coherence), $\gamma_{spatial}$ is spatial baseline decorrelation, $\gamma_{temporal}$ is temporal decorrelation, $\gamma_{Doppler}$ is Doppler centroid decorrelation, and $\gamma_{thermal}$ is thermal decorrelation. Total correlation is 1 when there is no decorrelation. The spatial baseline decorrelation is related to the horizontal separation between two satellite orbits. Doppler centroid related decorrelation effects occur when the satellite attitude (yaw, roll, pitch) is different during master and slave acquisitions. The effect is due to the squint angle ($\Psi$), which is dependent on the yaw and pitch of the satellite (Miranda et al., 2003). Temporal decorrelation occurs when the physical properties of scatterers in a resolution cell changes over time. Temporal decorrelation is stronger in forests where volume scattering is dominant. Thermal noise of the radar also creates a decorrelation term and is generally neglected for interferometry.

As shown in Eq. (1.2) interferometric phase is a sum of many phenomena such that errors in satellite position, and topography alter deformation measurements. Furthermore, changing atmospheric conditions also degrade the deformation signal. Since 2000, many groups worked on mitigating these unwanted signals, using multiple acquisitions over the same area (Ferretti et al., 2000, 2001, 2009c, 2011; Berardino et al., 2002; Werner et al., 2003; Hooper et al., 2004; Kampes, 2005, 2006; Lanari et al., 2007; Blanco-Sanchez et al., 2008; Costantini et al., 2008, 2012; Crosetto et al., 2008; Kuehn et al., 2010; Perissin and Wang, 2012). Aside from these deterministic phase contributions, unwrapping of interferometric phase is a non-deterministic problem that has many equally correct solutions, and can only be solved under certain assumptions (Bioucas-Dias and Valadão, 2007). These assumptions change among time series algorithms that are reviewed in this paper.

## 2. Phase unwrapping

InSAR phase measurements are wrapped between $-\pi$ and $+\pi$. For most practical applications continuous phase values are required, and are called unwrapped phase (Fig. 2). Regardless of being defined in 2D or 3D, unwrapped phase is the continuous curve of the argument of the measured data, and can be rigorously defined as an integral of the phase derivative, with the initial condition that the argument of the starting point is zero as shown in Eq. (2.1) (Tribolet, 1977).

$$\varphi_N = \int_{m=0}^{N} \varphi'_m dm \tag{2.1}$$
$$\varphi_0 = 0$$

where $\varphi_0$ is the reference point, $\varphi_N$ is the end point, $m$ is the integration variable (samples along measurement axis), and $\varphi'_m$ is the complex phase derivative. Because InSAR measurements are

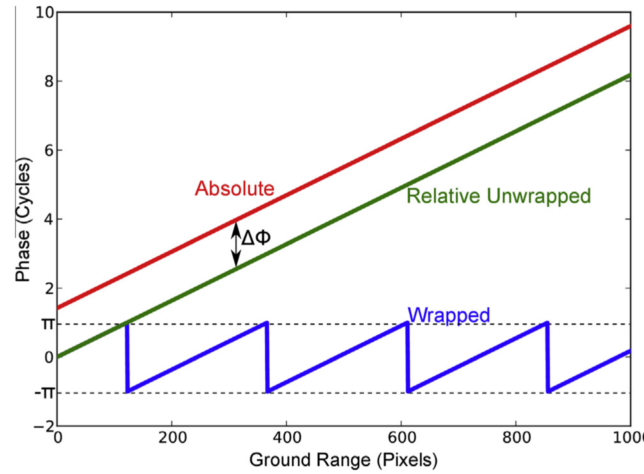


**Fig. 2.** The wrapped phase (blue), relative unwrapped phase (green) and absolute phase (red). (Modified from Massonnet and Feigl, 1998). (For interpretation of the references to color in this figure legend, the reader is referred to the web version of this article.)

relative, the offset ($\Delta\varphi$) between absolute phase and relative unwrapped phase can only be resolved using additional information, such as GPS measurements.

There are other definitions of the phase unwrapping operation in the literature. Unwrapping is also defined as sum of the complex-wrapped differences of the principal values (Ghiglia et al., 1987; Itoh, 1982):

$$\varphi_N = \varphi_0 + \sum_{m=0}^{N} \Delta\varphi_m \tag{2.2}$$

where $\Delta\varphi_m$ is the phase of discrete complex derivative operation ($angle(\Delta e^{i\varphi_m})$). For the discrete case the only practical difference between Eqs. (2.1) and (2.2) is the value of the initial pixel, where it is set to zero in Eq. (2.1), but set to the angle of the initial pixel in Eq. (2.2). An expansion of these unwrapping functions to multiple dimensions can be found in Osmanoglu et al. (2011a).

### 2.1. Review of phase unwrapping algorithms

One of the first unwrapping algorithms was introduced almost four decades ago by Tribolet (1977). Since then several unwrapping algorithms have been developed. For two or more (e.g. 3-D) dimensions these unwrapping algorithms can be separated into two groups: (1) path-following and (2) path-independent algorithms. Path-following unwrapping algorithms follow a path in the wrapped phase and unwrap each pixel locally. The path-independent unwrapping algorithms take a more global approach and minimize some measure of misfit between the unwrapped solution and wrapped phase gradients (Ghiglia and Pritt, 1998).

#### 2.1.1. Path following unwrapping algorithms

There are many different path following unwrapping algorithms in the literature, including but not limited to: Goldstein et al., 1988; Bone, 1991; Ghiglia and Pritt, 1998; Xu and Cumming, 1999; Krämer, 1998; Kim and Griffiths, 1999; Herráez et al., 2002; Abdul-Rahman et al., 2007; Loffeld et al., 2008; Martinez-Espla et al., 2009; Navarro et al., 2012. All these algorithms utilize a local unwrapping function, and unwrap all the pixels one-by-one starting from a reference point. The phase of the reference point is either known *a priori* or assumed to be zero.

Sequential paths are the simplest paths used for path-following unwrapping methods. Sequential paths do not use quality (or cost) maps to define a preferred path, and any area-filling (2-D) or volume-filling (3-D) curve can be used to define a sequential path. These paths are generally combined with filter based unwrapping functions, which can reduce noise induced errors effectively during the unwrapping operation (Krämer, 1998; Loffeld et al., 2008; Martinez-Espla et al., 2009; Navarro et al., 2012).

One of the first and more popular phase unwrapping algorithms for 2-D data was Goldstein's branch-cut algorithm (Goldstein et al., 1988). Branch-cut theory defines "residues", which are local errors caused by noise or discontinuities in the data. Residues are calculated using a rotational sum of phase differences over the data and can be either positive or negative (Goldstein et al., 1988; Chen and Zebker, 2000; Bamler and Hartl, 1998). A "branch-cut" is placed between residues with opposite signs or between the edge of the image and a residue. An unwrapping path that does not go through any residues can then be calculated, providing a unique (non-ambiguous, path independent) solution. However there are many different ways to draw branch-cuts, and several papers have been written on the topic using different methods: nearest neighbor (Goldstein et al., 1988; Zheng and Da, 2011), minimum cost matching (Buckland et al., 1995), stable marriages (Quiroga et al., 1995), modified nearest neighbor (Cusack et al., 1995), phase field direction (Gutmann and Weber, 2000), and residue vector approach (Karout et al., 2007). Branch-cut algorithm has since been applied to 3-D unwrapping as well, for which 2-D branch-cut surfaces are defined (Huntley, 2001; Cusack and Papadakis, 2002; Salfity et al., 2006; Hooper and Zebker, 2007).

Another class of path-following unwrapping algorithms are defined using quality or cost maps. While quality maps show the quality of individual pixels with respect to others, cost maps define a "penalty" value for using a certain pixel in the solution. Even though these two maps show opposite values, the idea behind them is similar when it comes to defining a path: use the high-quality (low-cost) pixels as soon as they become available, and delay unwrapping of low-quality (high-cost) pixels. Unwrapping paths employing quality or cost maps can also incorporate branch-cuts to the path resulting in a combined algorithm.

#### 2.1.2. Path-Independent unwrapping algorithms

Path independent unwrapping algorithms find a global solution minimizing a certain measure of misfit between the wrapped data and unwrapped solution. Because the algorithm operates globally on the complete dataset, no unwrapping path is required. An important class of path-independent unwrapping algorithms is the minimum $L-p$ norm, which also includes least squares ($L-2$ norm).

$L-p$ norm algorithms operate with the assumption that there should be a small misfit between the derivative of the unwrapped data, and complex phase derivative obtained from the wrapped data (Ghiglia and Romero, 1996):

$$|X|^p = \sum_{k=1}^{N} \left| (\hat{\varphi}_k - \hat{\varphi}_{k-1}) - \arg(\varphi_k \varphi^*_{k-1}) \right|^p \tag{2.3}$$

where $|X|^p$ is the misfit, $N$ is the total number of pixels, $\hat{\varphi}$ is unwrapped phase estimate, $\varphi$ is wrapped phase, and $p$ is the degree of the norm. Helmholtz decomposition can separate any vector field into rotational and irrotational, parts suggesting that Eq. (2.3) should satisfy zero rotational field condition (no residues) as follows (Ghiglia and Pritt, 1998):

$$\nabla \times \nabla_{\varphi} = 0 \tag{2.4}$$

where the $\nabla \times \nabla$ denotes the curl operator and $\varphi$ is the wrapped phase. Following the Helmholtz decomposition, if the rotational part is zero, the $L-p$ norm solution reduces to the following Poisson's equation (Ghiglia and Romero, 1994; Chen, 2001):

$$\nabla^2 \hat{\varphi} = \nabla^2 \varphi \tag{2.5}$$

where $\nabla^2$ indicates the Laplacian operator, $\hat{\varphi}$ is the estimated unwrapped phase, and $\varphi$ is the wrapped phase. The right side of Eq. (2.5) can be calculated directly from the wrapped phase values. When $p = 2$ and no weighting is used the solution of Eq. (2.3) is equivalent to solving Poisson's equation (Eq. (2.5)) with Neumann boundary conditions (Ghiglia and Romero, 1996). The Neumann boundary conditions state that the derivative of the unwrapped phase is equal to the angle of complex phase multiplication. Without weighting ($p = 2$), the Laplacian operation is equivalent to convolution of the following kernel on the left side of Eq. (2.5).

Using the relations between convolution in time domain and multiplication in frequency domain (convolution theorem), the Laplacian kernel can be deconvolved from the right side of the equation by division in the frequency domain. Hence the solution can be achieved using 2-D discrete cosine transforms or fast Fourier transforms (Ghiglia and Romero, 1994; Pritt and Shipman, 1994). However, if residues exist, the rotational field ($\nabla \times \nabla_{\varphi}$) is not zero (see Eq. (2.4)), and the $L-p$ norm algorithms will underestimate the signal, often indicated by missing fringe lines (Xu and Cumming, 1999; Loffeld et al., 2008). Residue-cut algorithms can be utilized to adjust weighting of weighted $L-p$ norm algorithms to reduce misfit. The residue cut algorithm was extended using the network theory to obtain an efficient solution to the phase unwrapping problem in 2-D (Flynn, 1997; Costantini, 1998; Chen and Zebker, 2000). In the network flow model, each $2 \times 2$ pixel is considered a node and the calculated residue value is used as an arbitrary commodity. The network is then balanced by satisfying the commodity supply and demand with the help of minimum cost flow theory. The SNAPHU, a statistical-cost network-flow algorithm for phase unwrapping, uses different statistical cost models for unwrapping problems of topography and deformation, combined with the network theory to obtain approximate L0 norm solutions.

Most InSAR unwrapping methods focus on unwrapping a single image, hence are 2-D. With the advent of multi-temporal InSAR, 3-D phase unwrapping gained importance. 3-D unwrapping can be achieved using 1 + 2D operations, where a series of 1-D and 2-D operations are consecutively used to unwrap the 3-D data. For example a popular path independent 1-D phase unwrapping method applied to phase history of a single pixel is called periodogram. Periodogram method tries to find the best fitting frequency and phase constant to a series of wrapped phase samples (Clarkson, 1999). The method relies on finding the maximum likelihood estimate for the periodogram, which is defined as:

$$\zeta(\mathrm{f}) = \left| \sum_{n=1}^{N} (e^{i\varphi})(e^{-i2\pi f n}) \right| \tag{2.6}$$

where $\zeta(f)$ denotes the periodogram at frequency $f$, $N$ is the number of periodogram samples, and $(e^{i\varphi})$ is the complex phase. Solution is generally achieved by calculating the periodogram using FFT, and finding the frequency maximizing the periodogram with a gradient descent algorithm (Clarkson, 1999). Periodogram is often combined with spatial (2-D) unwrapping to constitute a solution for unwrapping of 3-D data.

## 3. Time series analysis of InSAR data

Time series analysis of InSAR data, which observes the displacement of the Earth's surface over time, is an indispensable tool for many fields of Earth science. Several algorithms have been developed for time series analysis of InSAR data (in alphabetical order): Coherent Pixels Technique (CPT) (Blanco-Sanchez et al., 2008); Delft Persistent Scatterer Interferometry (DePSI) (Kampes, 2005, 2006); Interferometric Point Target Analysis (IPTA) (Werner et al., 2003); Permanent Scatterer InSAR (PSInSAR™) (Ferretti et al., 2000, 2001); Persistent Scatterer Pairs (PSP) (Costantini et al., 2008, 2012); Quasi Persistent Scatterers (QPS) (Perissin and Wang, 2012); Small Baseline Subset (SBAS) (Berardino et al., 2002; Lanari et al., 2007); Stable Points Network (SPN) (Crosetto et al., 2008; Kuehn et al., 2010); SqueeSAR™ (Ferretti et al., 2009c, 2011); and Stanford Method for Persistent Scatterers (StaMPS) (Hooper et al., 2004; Hooper, 2008).

Fig. 3 shows the average number of citations for the most popular reference of the technique, and the average number of papers referring to the technique based on Google Scholar, Scopus and Web of Science. PSInSAR™ is the most cited technique, while IPTA has the most publications, even though it is possible to change these numbers somewhat by using different keywords in the search engine. All these techniques aim to connect wrapped phase measurements to produce a near continuous record of displacement. Despite their common goal of producing an unwrapped time series of InSAR phase observations, these algorithms have important theoretical and practical differences. For instance, some algorithms rely mostly on persistent scatterers, while others focus on distributed scatterers.

The distributed and persistent scatterers have real physical differences, such as the size of the target relative to the resolution cell and reflected power. Differences in target behavior give rise to different algorithms to solve for surface deformation. General procedure of each algorithm is outlined together with an example to demonstrate their similarities and differences.

### 3.1. Persistent Scatterer Interferometry (PSI)

PSI, PSInSAR™, and IPTA share the same basic theory. For the sake of simplicity, in this section all of these algorithms will be referred to as PSI. In the science community the technique is referred as PSI in order not to infringe on the PSInSAR™ trademark. The PSI time series algorithm was developed to use the persistent scatterers (PS), which are scatterers that have dimensions smaller than the SAR resolution cell (Ferretti et al., 2001; Kampes, 2006). Therefore, PS are not affected by baseline decorrelation, and a single master stack of interferograms can be formed even if the baselines are longer than the critical baseline, which results in phase decorrelation for distributed scatterers. Without baseline decorrelation all acquired data can be used to form interferograms, which is a key advantage of this algorithm. On the PS it is possible to achieve sub-meter DEM precision and a surface motion precision of a few millimeters (Ferretti et al., 2007b).

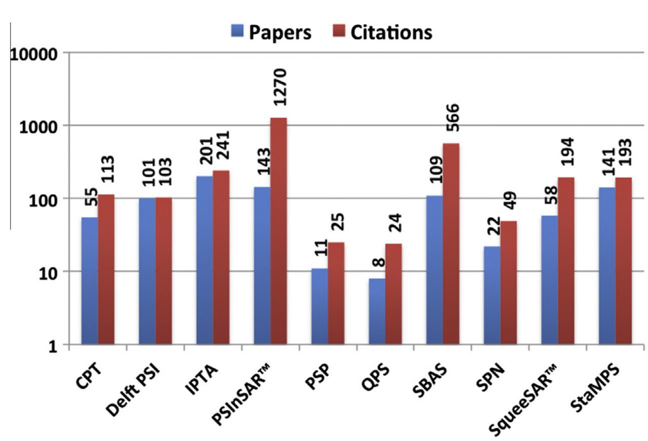


**Fig. 3.** Popularity of different InSAR time series methods covered in this study. *Y*-axis is in logarithmic scale to show the wide range. Exact paper and citation numbers are shown above each column.

The PS can be geolocated more accurately and a residual DEM error can be calculated after the initial DEM subtraction. Several types of PS can be distinguished from each other, and provide a way of locating the points in the resolution cell (Perissin and Ferretti, 2007). Because PS are more abundant in urban environments, PSI is a suitable method for time series analysis in metropolitan areas (Soergel, 2010).

The main processing steps of PSI are:

1. Generation of single master stack interferograms and removal of topographic phase.
2. Selection of candidates based on amplitude dispersion method.
3. Estimation and removal of atmospheric phase screen (APS).
4. Finding additional PS.

Generation of the single master stack interferograms and removal of topographic phase from each interferogram is accomplished using an InSAR processing software, like DIAPASON, DORIS, ISCE, ROI-PAC, etc. It is important to note that due to large baselines some interferograms will not have visible fringes, but pixels containing PS will remain coherent.

Persistent scatterer candidates (PSC) are points that are a first step approximation to PS based on predefined selection criteria. The amplitude dispersion method selects the PSC based on the scatterer amplitude value over time. The idea is that given the same level of noise applied to a strong (high amplitude) scatterer and a weak (low amplitude) scatterer the phase change due to the same amount of noise will be much less in the strong scatterer, as shown in Fig. 4. The amplitude dispersion of an individual pixel is defined as the ratio of its standard deviation to its mean value and can be calculated as follows (Ferretti et al., 2001):

$$D_A = \sigma_A / \mu_A \tag{3.1}$$

where $D_A$ indicates the amplitude dispersion value, and $\sigma_A$ and $\mu_A$ indicate standard deviation and mean of amplitude values. Typically, points with a $D_A$ of less than 0.25 are selected as PSC.

Corrected values for DEM and estimates of deformation velocities are calculated for the selected points by the amplitude dispersion method using an iterative calculation starting from the small baseline interferograms. The next step is to calculate atmospheric phase screen (APS), which starts with the estimation of the master APS. A 2-D spatial network is formed using the PSC and residual phase values are calculated for each PSC after the DEM ($\varphi_{topo}$) and deformation ($\varphi_{defo}$) signals are removed. This remaining

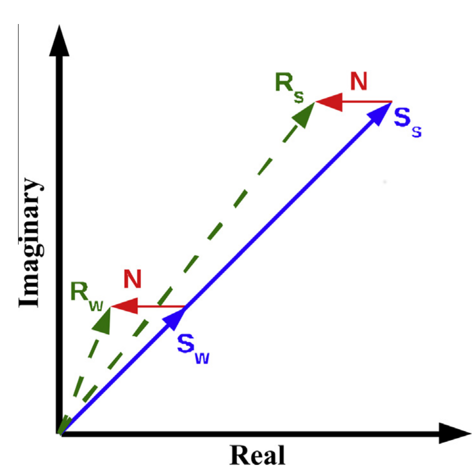


**Fig. 4.** Amplitude of weak ($S_W$) and strong ($S_S$) scatterers are indicated by the vector length. When the same noise $N$ is applied to both scatterers, the phase angle of the resulting vector for the weak scatterer ($R_W$) changes more than that of the strong scatterer ($R_S$).

residual phase includes the phase contributions of $\varphi_{atmo}$, $\varphi_{scat}$, and $\varphi_{noise}$ as in Eq. (1.2). For the PSC the changes in the dielectric constant of the scatterer ($\varphi_{scat}$) can be neglected. Since the interferograms are formed as a single master stack, all interferograms have the atmospheric contribution from the master acquisition, which can be estimated by an average of the residual. Once the $\varphi_{atmo}$ for all the PSC in the master acquisition is known, a low pass filter and Kriging operation are applied in space domain to calculate APS for the master acquisition. The APS for other acquisitions can be calculated in the same way, allowing removal of $\varphi_{atmo}$ from all interferograms. All PSI techniques require a larger number of scenes available (>10) for reliable solution, especially in case of inaccurate baselines and topographic height maps to estimate the atmospheric phase screen correctly (Werner et al., 2003; Kampes and Hanssen, 2004).

After the APS calculation, all unwanted signals can be removed from the observation and DEM errors and scatterer velocity can be calculated on a pixel-by-pixel basis for all points. This operation is done using a time series analysis of the phase values maximizing the coherence value. For the high SNR case and with >30 acquisitions, the expected DEM accuracy for the PS is 0.5 m and the deformation rate precision is 0.5 mm/yr (Ferretti et al., 2001).

Several variations of the PSI algorithm have been developed over the past years. SPN, and PSP are two examples and their differences are mentioned in the following sections.

#### 3.1.1. Stable point network (SPN)

PSI algorithms use a single master stack because by definition the PS are not affected by baseline decorrelation. Even though SPN utilizes persistent scatterers, it uses a multi-master stack aimed at limiting the geometric decorrelation for imperfect PS. SPN can select persistent scatterers using three different selection criteria: amplitude stability; interferometric coherence; and spectral coherence which is to be used when only a few scenes are available and processing has to be done at full resolution (Crosetto et al., 2008). SPN is built on the DIAPASON interferometric processor, which is developed by CNES since 1992 (Duro et al., 2004). SPN has been successfully applied to several ground deformation phenomena (Crosetto et al., 2008; Kuehn et al., 2010; Herrera et al., 2011).

#### 3.1.2. Persistent scatterer pairs (PSP)

PSI relies on accurate estimation and removal of spatial artefacts, like orbital ramps, atmospheric phase contribution and DEM errors. To achieve this, a large number of scenes and a deformation model, which is generally defined to be linear, are used. The persistent scatterer pairs method, relaxes the necessity of the deformation model, by introducing an assumption such that the spatial artefacts are correlated in space, and can be ignored when comparing neighboring points. PSP defines arcs using neighboring points, and constructs a network defining all the potential PS with a minimum set of arcs (Costantini et al., 2010). For each arc, the difference in height and deformation velocity is calculated over the network, which can later be integrated to obtain an unwrapped solution using finite difference integration (Costantini et al., 2012).

*3.1.2.1. Application (Osmanoglu et al., 2011b).* Subsidence in Mexico City has been studied with PSI (Osmanoglu et al., 2011b) using an earlier version of Delft PSI Toolbox (DePSI). In an urban setting like Mexico City, PSI is a natural choice for deformation analysis due to abundance of persistent scatterers. In this analysis GPS stations (Fig. 5) were used to validate the PSI results. The GPS station shown as white in Fig. 6 is used as a tie-point between GPS and PSI deformation rates, achieving a RMS agreement of 6.9 mm/yr. The maximum observed line of sight rate is over 30 cm/yr.

### 3.2. Stanford Method for Persistent Scatterers (StaMPS, a.k.a. MAINSAR)

StaMPS has some similarities with the PSI method, however, the persistent scatterers are redefined as scatterers with stable phase

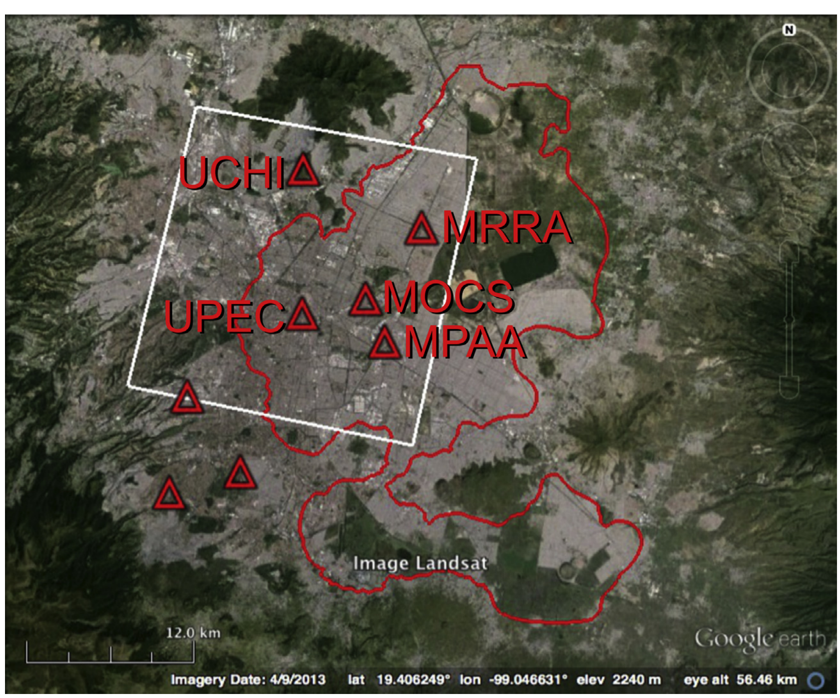


**Fig. 5.** Satellite image of Mexico City. White rectangle shows the study area common to Figs. 6, 7, 10 and 11. Red boundary shows the limit of clay-rich lacustrine sediments from former Lake Texcoco that is prone to consolidation. Red triangles show the locations of continuous GPS stations. (For interpretation of the references to color in this figure legend, the reader is referred to the web version of this article.)

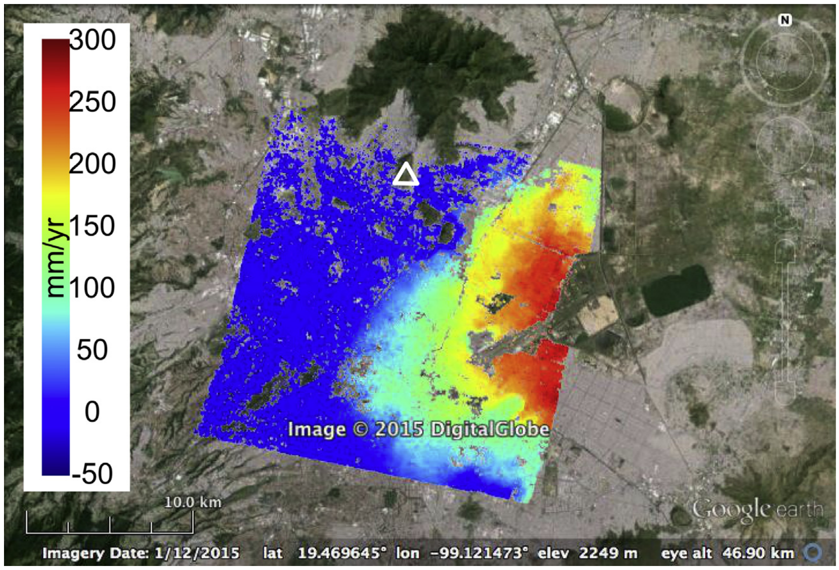


**Fig. 6.** Results using PSI over Mexico City between January 2004 and July 2006. The white triangle indicates the location of the UCHI continuous GPS station used as the reference point for PSI analysis (Osmanoglu et al., 2011b). This reference point was chosen because it is outside of the subsiding area.

characteristics in space and time regardless of their amplitude (Hooper et al., 2004). Therefore, even though the points are called persistent scatterers like in PSI, the meaning of the term only agrees in regards to the phase characteristics and not in the method for finding these points. This change allows use of StaMPS over non-urban terrain to measure deformation.

StaMPS and PSI both utilize amplitude dispersion for the initial selection of PSC, but the threshold value for StaMPS is higher (0.4). StaMPS also employs an iterative model, where coherence of the PSC are calculated using other nearby PSC and points with low coherence values are rejected. PSI only selects PSC with a stable temporal behavior, eliminating more points than StaMPS. Furthermore, the model for finding additional PS is different. In PSI, the model is a combination of the topography, linear phase, and long wavelength error sources (atmosphere and orbit), whereas in StaMPS the only constraint is phase variance of the phase in a local window (Kampes, 2006; Hooper et al., 2004; Sousa et al., 2009).

The way the unwrapping operation is handled has changed since the initial version of StaMPS was released. The initial version employed a series of 2-D unwrapping operations to generate the 3-D time series. The unwrapping was first done in time domain and then an iterative least square method was used to integrate a 3-D solution over all the samples. The latest version of the StaMPS is 3.3b1, released 12 September 2013, while StaMPS comes with a 3-D unwrapping method since version 2.0, that consists of estimating the probability density functions in space dimension after temporal unwrapping, interpolating the sparse points to a regular grid, and defining cost-maps to optimize spatial unwrapping achieved

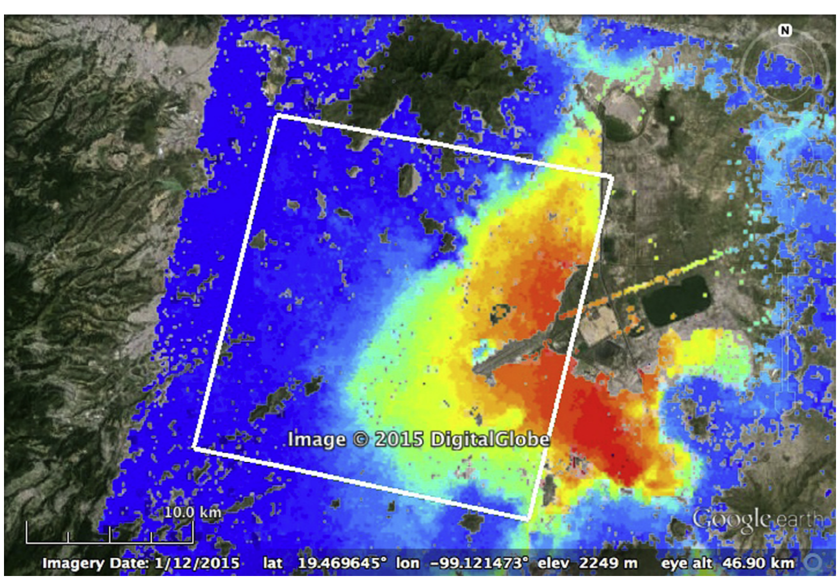


**Fig. 7.** Deformation map of Mexico City, obtained by StaMPS using Envisat data between 2002 and 2010. (modified from Siles et al., 2015). The white outline marks the study area common to all results. The color scale is the same as Fig. 6. (For interpretation of the references to color in this figure legend, the reader is referred to the web version of this article.)

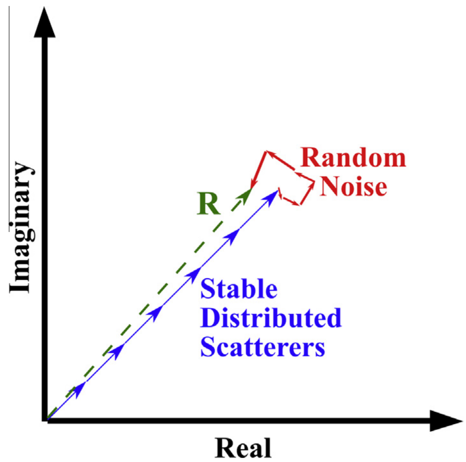


**Fig. 8.** Distributed scatterers can be coherently summed to reduce the effect of random noise on the signal of interest.

by SNAPHU) (Hooper et al., 2009; Hooper, 2009). Since version 3.0, StaMPS allows for analysis of distributed scatterers with small baselines method (Section 3.3), as well as combining the PS and SBAS solutions.

*3.2.1. Coherence Pixel Technique (CPT)*

Coherent pixel technique is similar to PSI methods, because it utilizes persistent scatterers for analysis and starts from wrapped interferograms. However CPT uses minimum spanning tree network in three dimensions with temporal, perpendicular and Doppler centroid frequency as three axes to form a multi-master stack of interferograms instead of a single master stack (Blanco-Sanchez et al., 2008). The interferometric phase is solved over the arcs, using an iterative optimization routing called conjugate gradient method (CGM). Non-linear deformation can be estimated using singular value decomposition after the interferograms are unwrapped with an initial linear model.

*3.2.1.1. Application (Siles et al., 2015).* Envisat ASAR data over Mexico City between 2002 and 2010 are analyzed with StaMPS to obtain deformation rate over the entire swath. The subsiding area shown in Fig. 7 agrees well with the clay rich lake sediment area

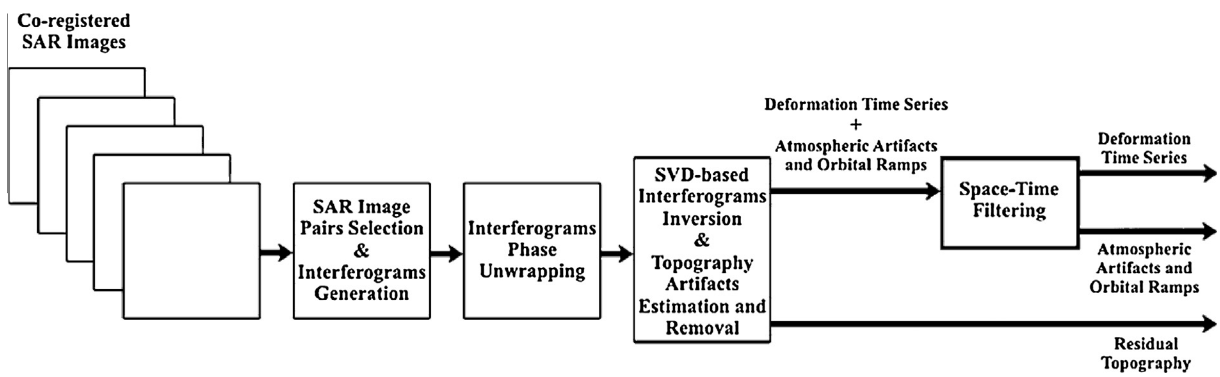


**Fig. 9.** Block diagram for SBAS algorithm (Lanari et al., 2007).

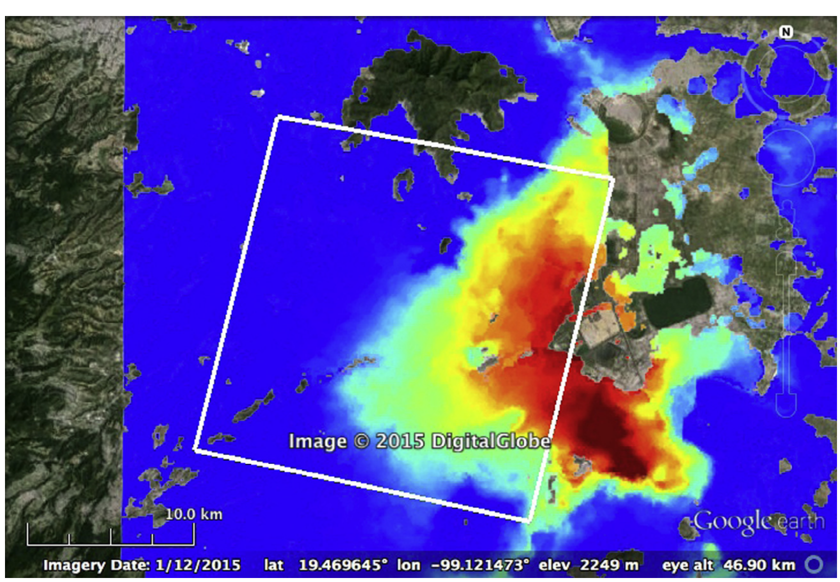


**Fig. 10.** Subsidence rate estimated by SBAS over Mexico City from 38 Envisat images between 2002 and 2007. Maximum subsidence rate is 38 cm/yr (modified from Yan et al., 2009). The white outline shows the comparison area, and the color scale is the same as Fig. 6. (For interpretation of the references to color in this figure legend, the reader is referred to the web version of this article.)

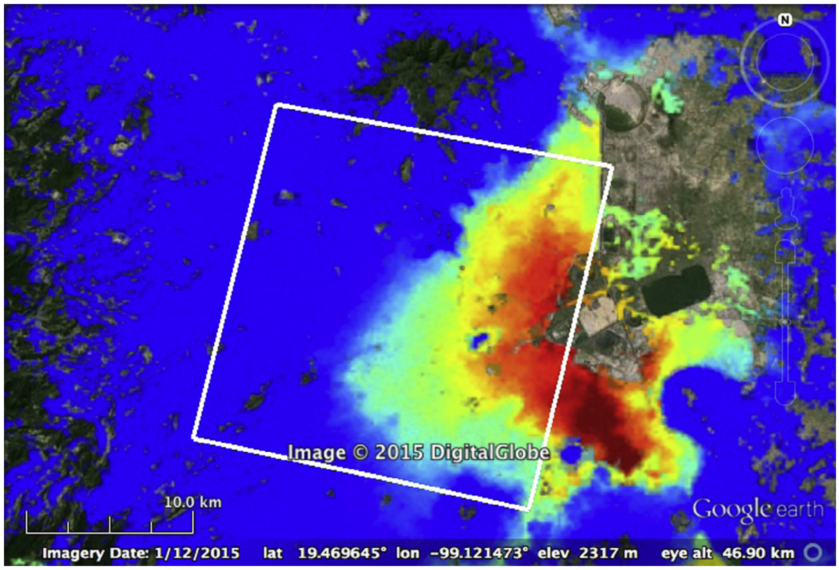


**Fig. 11.** SqueeSAR subsidence map of Mexico City using Envisat data between 2003 and 2010. (Hernández-Espriú et al., 2014). White polygon outlines the comparison area. The color scale is the same as Fig. 6. (For interpretation of the references to color in this figure legend, the reader is referred to the web version of this article.)

shown in Fig. 5. The high point density in the urban area allows for analysis over large structures such as the elevated Metro line (Siles et al., 2015).

### 3.3. Small Baseline Subset (SBAS)

The SBAS algorithm uses distributed scatterers (Fig. 8) and singular value decomposition to connect independent unwrapped interferograms in time (Berardino et al., 2002; Lanari et al., 2004). Small Temporal Baseline Subset (STBAS) is a modification to the SBAS algorithm in which only interferograms with short temporal baselines are used (Hong et al., 2010; Hong and Wdowinski, 2014). The short temporal baselines are especially needed for highly variable phenomena, such as monitoring water level changes in wetlands, to minimize temporal decorrelation. Due to their underlying conceptual similarities, both algorithms are referred to as SBAS for the purposes of this paper.

SBAS combines multiple unwrapped interferograms to generate a time series. The master and slave pairs for these interferograms are selected using the average baseline parameters for the signal of interest. For deformation analysis, baseline parameters can be set to 25% of the critical baseline (~400 m), and ~1 year for temporal baseline. In the case of the STBAS algorithm, the shortest temporal baseline pairs are selected regardless of the spatial separation. As shown in Fig. 9, these interferograms have to be coregistered to a single image.

Unwrapped, coregistered interferograms include topography, atmosphere and deformation signals. The topography signal is included in all the interferograms, even though it is scaled by the perpendicular baseline. Topography can be calculated by combining all the interferograms as follows (Berardino et al., 2002):

$$\Delta_z = \left[\frac{4\pi B_{\perp 1}}{\lambda R sin\theta}\,\frac{4\pi B_{\perp 2}}{\lambda R sin\theta}\cdots\frac{4\pi B_{\perp N}}{\lambda R sin\theta}\right] \tag{3.2}$$

where $\Delta_z$ is the topography relative to the reference point, $B_\perp$ is perpendicular baseline for each acquisition, $R$ is range and $\theta$ is antenna look angle. After defining and removing topographic phase contribution, the signal only contains atmospheric and deformation signals. The resulting interferograms are converted into mean phase velocities between time-adjacent acquisitions (Berardino et al., 2002). Atmospheric filtering is done at the end of the processing by extracting the signal with high spatial and low temporal correlation using a spatio-temporal filter, as is the case for PSI (Ferretti et al., 2000, 2001).

#### 3.3.1. Application (Yan et al., 2009)

38 Envisat ASAR images acquired over Mexico City between November 2002 and March 2007 were analyzed to obtain subsidence rate using SBAS and Delft PSI techniques (Yan et al., 2009, 2012). Both methods achieve similar results with majority of the points showing less than 2 cm/yr difference between SBAS and PSI results. The deformation rate obtained by SBAS is shown in Fig. 10, with 5 cm/yr wrapping, reaching a maximum of −38 cm/yr. Yan et al. (2012) note difficulties in spatial unwrapping of some interferograms for the SBAS algorithm. Incoherent areas are masked out and shown as white in Fig. 10. They further note that the non-linear portion of the deformation were not captured using PSI, due to the linear model assumption (Yan et al., 2009, 2012).

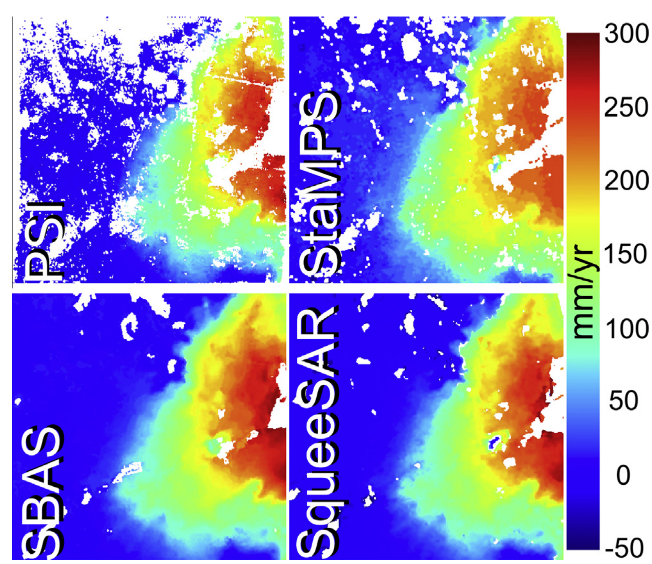


**Fig. 12.** Comparison between results obtained from PSI, StaMPS, SBAS and SqueeSAR algorithms cropped to the study area. The time spans for the data are not exactly the same.

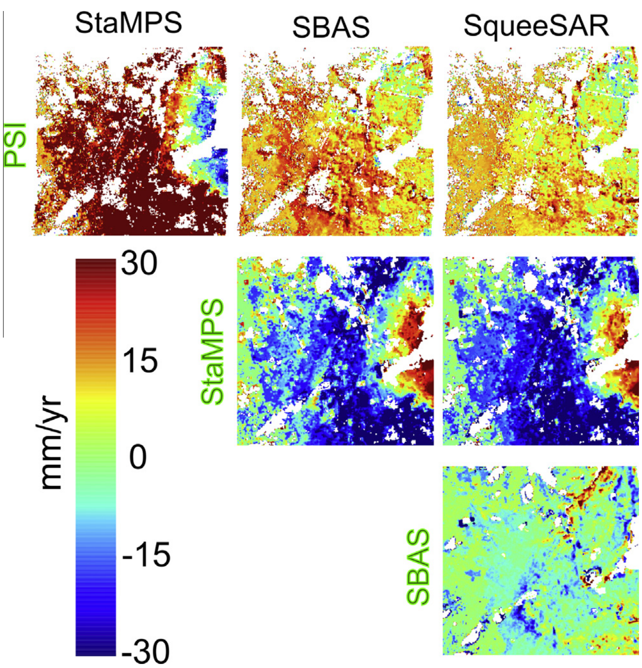


**Fig. 13.** Maps with residual velocities representing the different results obtained by the four methods. The method name in rows (green) is subtracted from columns (black). For example first box shows the result of PSI subtracted from StaMPS. (For interpretation of the references to color in this figure legend, the reader is referred to the web version of this article.)

### 3.4. SqueeSAR™

The SqueeSAR is advertised as the second generation PSInSAR™ by it's developer, TRE (Ferretti et al., 2009a–c, 2011). The main difference of SqueeSAR from it's predecessor is the combination of persistent and distributed scatterers for the time series analysis. In other words, while PSI was focusing on solely persistent scatterers, SqueeSAR combines information from both distributed and persistent scatterers (Rocca et al., 2013). Combination of persistent and distributed scatterers is achieved by constructing a multi-master network, and defining a new distance metric, to find the correct grouping of points in the same spatial neighborhood in a stack of interferograms. The distance metric used in SqueeSAR is the Kolmogorov–Smirnov (KS) test (Ferretti et al., 2009b; Parizzi and Brcic, 2011). The non-parametric KS test uses the maximum value of absolute difference between two cumulative distribution functions (CDF) as it's metric (Parizzi and Brcic, 2011). The KS test used in the SqueeSAR uses amplitude values from a stack of interferograms to calculate the probability density function and CDF. Pixels are then combined with their neighboring pixels with similar CDF (or with low KS distance), creating neighborhoods.

#### 3.4.1. The Quasi-PS technique (QPS)

Quasi-PS utilizes partially coherent targets in order to increase the spatial density of the observations. However, instead of the single master stack used in most persistent scatterer algorithms, it uses a multi-master network to limit the baseline decorrelation. Furthermore this allows for incorporation of temporally coherent scatterers (Quasi-PS), allowing for increased coverage in non-urban areas. Another difference from the regular PSI algorithms is that spatial filtering can also be applied to improve the phase response of the distributed scatterers. Unlike SqueeSAR, QPS does not use a statistical similarity measure to group the distributed scatterers (Luo et al., 2012).

*3.4.1.1. Application (Hernández-Espriú et al., 2014).* SqueeSAR was used to analyze the subsidence in Mexico City using Envisat data between 2003 and 2010. The annual subsidence rate was calculated by averaging the total subsidence rate over the entire time span. The maximum subsidence rate was found to be 343 mm/yr in line-of-sight direction (Fig. 11, Hernández-Espriú et al., 2014).

### 3.5. Comparison of the methods

In order to evaluate the similarities and differences between the four methods, we compared their results in the common study area that was first used by Osmanoglu et al. (2011b) by plotting all four solutions in one figure (Fig. 12). The four methods yielded

**Table 1**
Line of sight deformation rates for GPS, PSI and SqueeSAR in mm/yr.

| | MRRA | MOCS | MPAA | UPEC |
|---|---|---|---|---|
| GPS | −242 | −156 | −193 | −84 |
| PSI | −254 | −165 | −208 | −85 |
| SqueeSAR | −263 | −190 | −222 | −87 |

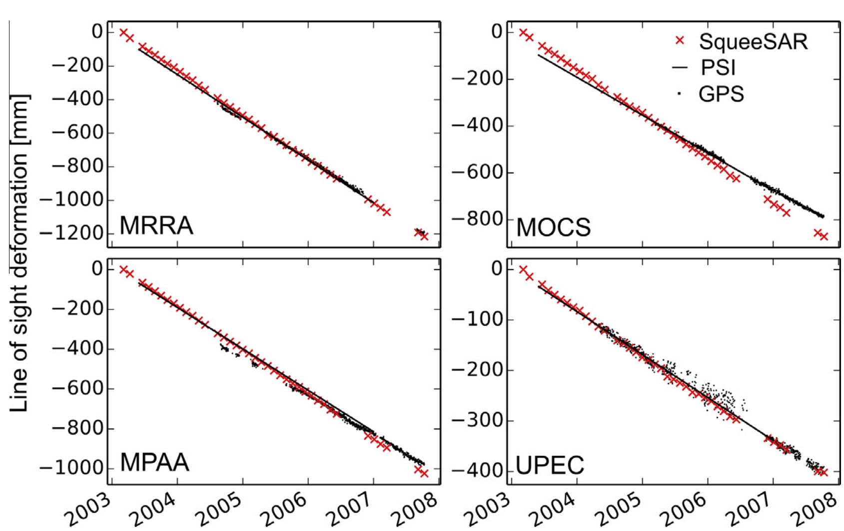


**Fig. 14.** Comparison of SqueeSAR, PSI and GPS timeseries. The locations of GPS stations are shown in Fig. 5.

**Table 2**
Comparison of InSAR time series methods (Modified from Lu and Dzurisin, 2014).

| Method | Phase | Element | Parameters | Network | Solver | Scatterer |
|---|---|---|---|---|---|---|
| CPT | Wrapped | Arc | $\Delta h$, $\Delta v$ | Multi-master | Conjugate gradient method | Point, distributed |
| Delft PSI | Wrapped | Arc | $\Delta h$, $\Delta v$ | Single master | Periodogram | Point |
| IPTA | Wrapped | Arc | $\Delta h$, $\Delta v$ | Single master | Periodogram | Point |
| PSInSAR™ | Wrapped | Arc | $\Delta h$, $\Delta v$ | Single master | Periodogram | Point |
| PSP | Wrapped | Arc | $\Delta h$, $\Delta v$ | Single master | Minimum cost flow | Point |
| QPS | Wrapped | Arc | $\Delta h$, $\Delta v$ | Multi-master | Periodogram | Point, distributed |
| SBAS | Unwrapped | Point | $h$, $v$ | Multi-master | Least squares | Distributed |
| SPN | Wrapped | Arc | $\Delta h$, $\Delta v$ | Multi-master | Periodogram | Point, distributed |
| SqueeSAR™ | Wrapped | Neighborhood | $\Delta h$, $\Delta v$ | Multi-master | Least squares | Point, distributed |
| StaMPS | Wrapped | Arc | $\Delta h$, $\Delta v$ | Multi-master | Minimum cost flow | Point, distributed |

a very similar subsidence pattern of high subsidence in the right-hand-side of the smaller study area with overall similar rates. The differences between the solutions were obtained by calculating residual velocity maps showing the differences between sets of two solutions (Fig. 13). This analysis yielded that maximum differences lie in the range of ±30 mm/yr, which is ~8% of the maximum subsidence rate. Smallest differences were obtained between the SBAS and SqueeSAR methods and largest between the StaMPS method with respect to all other. It is important to note that some differences in the velocities may arise from the use of different datasets in term of number observations and their time span.

A comparison of GPS timeseries, SqueeSAR and PSI timeseries are shown in Fig. 14. The SqueeSAR timeseries solves for acceleration, while the PSI result only accounts for linear motion. However it is clear from Fig. 14 that the subsidence in Mexico City is linear between 2003 and 2008. The GPS rates are converted to line-of-sight using satellite incidence and track heading angles (Osmanoglu et al., 2011b). All timeseries are offset in $y$-axis to match the SqueeSAR start day of March 7th, 2003. The rates for the given timeseries are shown in Table 1.

As a result of their distinct methods and features, each of the time series unwrapping algorithms is best matched to a particular set of conditions. For instance, PSI uses "persistent scatterers" in the observation area that are much smaller than the actual pixel resolution of the radar instrument. The scatterers are thus not affected by baseline decorrelation, and interferograms with very long baselines can be used to construct the time series. The abundance of permanent scatterers in urban areas makes PSI a useful technique for monitoring surface motion in urbanized areas (Colesanti et al., 2003; Bell et al., 2008; Bürgmann et al., 2006; Osmanoglu et al., 2011b). In contrast, SBAS and StaMPS unwrapping methods utilize mainly "distributed scatterers"; these can be affected by baseline decorrelation, but are more numerous in non-urban areas (Hooper, 2006; Gourmelen et al., 2007, 2010). Combining both permanent and distributed scatterers, SqueeSAR is a newer method for creating time series analyses, and has applications in a variety of study areas. A summary of the methods mentioned in this paper can be found in Table 2.

## 4. Conclusions and future trends

In this paper, four different results describing the Mexico City ground subsidence have been compared, which were achieved by different scientists using different techniques. The high subsidence rate of Mexico City provides a strong interferometric signal. Because the signal is very strong it is hardly suppressed by long-wavelength orbital errors, or the atmospheric phase screen. However, the high subsidence rate also increases the fringe rate observed in interferograms making it challenging to unwrap. All four algorithms obtain similar subsidence rates, and deformation patterns. The variations in deformation rates can be due to different assumptions in different algorithms, as well as the difference in the time period studied at each case. PSI, SBAS and SqueeSAR achieve similar rates over the study area, while the StaMPS approach shows a lower rate. Mexico City subsidence is highly linear through time, and therefore the rate differences are more likely to be the result of algorithmic differences rather than reflecting actual ground subsidence variations. It is also interesting that none of the methods were able to obtain deformation rates for the North-Eastern part of the study areas, around lake Nabor Carrillo. This area is home to agricultural farmlands and natural vegetation, which do not provide persistent scatterers. Furthermore due to farming activities (vegetation growth, harvesting, etc.) the signal is not reliable in the longer time scales. Extracting information from such areas remain a challenge, and might be solved with methods using shorter time frames, such as STBAS or algorithms focusing on partially (quasi) coherent targets. Until recently time series analysis and phase unwrapping have generally been treated as two separate areas of study, presumably because it is difficult to simultaneously solve all three dimensions observed with InSAR: the two spatial domains (termed azimuth and range) and time. In theory, however, an unwrapping algorithm could solve for signal ambiguity in all three dimensions, with significant advantages in terms of computing speed and robust analysis. Indeed, the time series analysis methods described in this paper can be considered unwrapping algorithms, with the added function of the atmospheric and spatial filtering operations that are included in some time series analysis algorithms.

Three-dimensional unwrapping algorithms have not been used until recently because of two main issues: (1) there are no efficient methods for solving phase ambiguity in three or more dimensions, unlike the case of two-dimensions, where unwrapping methods are based on network theory (Chen and Zebker, 2000, 2001, 2002); (2) larger datasets prohibit so-called "brute-force inversion" approaches. Path-following unwrapping methods unwrap the dataset pixel-by-pixel, making them well adapted for parallelization for improved speed, and limiting required memory to a relatively small amount. The disadvantage of path-following unwrapping is path dependence, as the algorithms can potentially diverge from the global minimum misfit solution by following a faulty "bad" path. Fortunately recent advances in the field provide solutions for unwrapping of sparsely distributed points in 3-D with certain assumptions (Shanker and Zebker, 2010; Hooper, 2010; Costantini et al., 2012). The future of InSAR relies on accurate unwrapping of 3-D data sets, as much as it relies on the continuation of InSAR capable satellites.

## Acknowledgements

The authors would like to thank ESA for making the Envisat data over Mexico City available through research grants. Part of this research was funded by NASA Grant NNX12AK23G. Authors would like to thank Penelope Lopez-Quiroz, and Gabriela Siles, for sharing their results and assistance. We kindly acknowledge TRE Canada Inc. for providing the SqueeSAR™ results on Mexico City.

## References


Abdul-Rahman, H., Gdeisat, M., Burton, D., Lalor, M., Lilley, F., Moore, C., 2007. Fast and robust three-dimensional best path phase unwrapping algorithm. Appl. Opt. 46 (26), 6623–6635.

Bamler, R., Hartl, P., 1998. Synthetic aperture radar interferometry. Inverse Prob. 14 (4), R1–R54.

Bell, J., Amelung, F., Ferretti, A., Bianchi, M., Novali, F., 2008. Permanent scatterer InSAR reveals seasonal and long-term aquifer-system response to groundwater pumping and artificial recharge. Water Resources Res. 44 (2) (Wo2, 407).

Berardino, P., Fornaro, G., Lanari, R., Sansosti, E., 2002. A new algorithm for surface deformation monitoring based on small baseline differential SAR interferograms. Geosci. Remote Sens. IEEE Trans. 40 (11), 2375–2383. http://dx.doi.org/10.1109/TGRS.2002.803792.

Bioucas-Dias, J.M., Valadão, G., 2007. Phase unwrapping via graph cuts. Image Process. IEEE Trans. 16 (3), 698–709.

Blanco-Sanchez, P., Mallorquí, J.J., Duque, S., Monells, D., 2008. The coherent pixels technique (CPT): an advanced DInSAR technique for nonlinear deformation monitoring. Pure Appl. Geophys. 165 (6), 1167–1193.

Bone, D.J., 1991. Fourier fringe analysis: the two-dimensional phase unwrapping problem. Appl. Opt. 30 (25), 3627–3632.

Buckland, J., Huntley, J., Turner, S., 1995. Unwrapping noisy phase maps by use of a minimum-cost-matching algorithm. Appl. Opt. 34 (23), 5100–5108.

Bürgmann, R., Hilley, G., Ferretti, A., Novali, F., 2006. Resolving vertical tectonics in the San Francisco bay area from permanent scatterer InSAR and GPS analysis. Geology 34 (3), 221.

Chen, C.W., Zebker, H.A., 2000. Network approaches to two-dimensional phase unwrapping: ıntractability and two new algorithms. J. Opt. Soc. Am. A 17 (3), 401–414.

Chen, C.W., 2001. Statistical-Cost Network-Flow Approaches to two-Dimensional Phase Unwrapping for Radar Interferometry, Ph.D. thesis, Stanford University. Dept. of Electrical Engineering.

Chen, C.W., Zebker, H.A., 2001. Two-dimensional phase unwrapping with use of statistical models for cost functions in nonlinear optimization. J. Opt. Soc. Am. A 18 (2), 338–351.

Chen, C.W., Zebker, H.A., 2002. Phase unwrapping for large SAR interferograms: statistical segmentation and generalized network models. Geosci. Remote Sens. IEEE Trans. 40 (8), 1709–1719.

Clarkson, I.V.L., 1999. Frequency estimation, phase unwrapping and the nearest lattice point problem. In: Acoustics, Speech, and Signal Processing, 1999. Proceedings, 1999 IEEE International Conference on, vol. 3, pp. 1609–1612.

Colesanti, C., Ferretti, A., Novali, F., Prati, C., Rocca, F., 2003. SAR monitoring of progressive and seasonal ground deformation using the permanent scatterers technique. Geosci. Remote Sens. IEEE Trans. 41 (7), 1685–1701.

Costantini, M., 1998. A novel phase unwrapping method based on network programming. Geosci. Remote Sens. IEEE Trans. 36 (3), 813–821. http://dx.doi.org/10.1109/36.673674.

Costantini, M., Falco, S., Malvarosa, F., Minati, F., 2008. A new method for identification and analysis of persistent scatterers in series of SAR images. In: Geoscience and Remote Sensing Symposium, 2008. IGARSS 2008. IEEE International, IEEE, vol. 2, pp. II-449.

Costantini, M., Falco, S., Malvarosa, F., Minati, F., Trillo, F., Vecchioli, F., 2010. Persistent scatterer pairs (PSP) approach in very high resolution SAR interferometry. In: Synthetic Aperture Radar (EUSAR), 2010 8th European Conference on, VDE, pp. 1–4.

Costantini, M., Malvarosa, F., Minati, F., 2012. A general formulation for redundant integration of finite differences and phase unwrapping on a sparse multidimensional domain. Geosci. Remote Sens. IEEE Trans. 50 (3), 758–768.

Crosetto, M., Biescas, E., Duro, J., Closa, J., Arnaud, A., 2008. Generation of advanced ERS and Envisat interferometric SAR products using the stable point network technique. Photogramm. Eng. Remote Sens. 74 (4), 443–450.

Cusack, R., Huntley, J.M., Goldrein, H.T., 1995. Improved noise-immune phase-unwrapping algorithm. Appl. Opt. 34 (5), 781–789.

Cusack, R., Papadakis, N., 2002. New robust 3-D phase unwrapping algorithms: application to magnetic field mapping and undistorting echoplanar images. Neuroimage 16 (3), 754–764.

DEOS, D., 2009. Doris User's Manual and Technical Documentation, Delft University of Technology, 4.02 ed.

Duro, J., Inglada, J., Closa, J., Adam, N., Arnaud, A., 2004. High resolution differential interferometry using time series of ERS and ENVISAT SAR data. In: FRINGE 2003 Workshop, vol. 550, p. 72.

Ferretti, A., Prati, C., Rocca, F., 2000. Nonlinear subsidence rate estimation using permanent scatterers in differential SAR interferometry. Geosci. Remote Sens. IEEE Trans. 38 (5), 2202–2212. http://dx.doi.org/10.1109/36.868878.

Ferretti, A., Prati, C., Rocca, F., 2001. Permanent scatterers in SAR interferometry. Geosci. Remote Sens. IEEE Trans. 39 (1), 8–20.

Ferretti, A., Monti-Guarnieri, A., Prati, C., Rocca, F., Massonet, D., 2007a. InSAR principles-guidelines for SAR interferometry processing and interpretation, vol. 19, chap. Part A, ESA Publications, ESTEC, Noordwijk, Netherlands.

Ferretti, A., Savio, G., Barzaghi, R., Borghi, A., Musazzi, S., Novali, F., Prati, C., Rocca, F., 2007b. Submillimeter accuracy of InSAR time series: experimental validation. IEEE Trans. Geosci. Remote Sens. 45 (5), 1142.

Ferretti, A., Fumagalli, A., Novali, F., Prati, C., Rocca, F., Rucci A., 2009a. High resolution InSAR with emphasis on complex scattering scenarios, presented at the Int. In: Geoscience Remote Sensing Symp. (IGARSS) Conf., Cape Town, South Africa.

Ferretti, A., Fumagalli, A., Novali, F., Prati, C., Rocca, F., Rucci A., 2009b. The Second Generation PSInSAR Approach: SqueeSAR, Presented at the Fringe Conf., Frascati, Italy.

Ferretti, A., Novali, F., Fumagalli, A., Prati, C., Rocca, F., Rucci, A., 2009c. Beyond PSInSAR: the SqueeSAR approach, in AGU Fall. Meet. Abstracts 1, 02.

Ferretti, A., Fumagalli, A., Novali, F., Prati, C., Rocca, F., Rucci, A., 2011. A new algorithm for processing interferometric data-stacks: SqueeSAR. Geosci. Remote Sens. IEEE Trans. 49 (9), 3460–3470.

Flynn, T.J., 1997. Two-dimensional phase unwrapping with minimum weighted discontinuity. J. Opt. Soc. Am. A 14 (10), 2692–2701.

Ghiglia, D.C., Mastin, G.A., Romero, L.A., 1987. Cellular-automata method for phase unwrapping. J. Opt. Soc. Am. A 4 (1), 267–280.

Ghiglia, D.C., Romero, L.A., 1994. Robust two-dimensional weighted and unweighted phase unwrapping that uses fast transforms and ıterative methods. J. Opt. Soc. Am. A 11 (1), 107–117.

Ghiglia, D.C., Romero, L.A., 1996. Minimum Lp-norm two-dimensional phase unwrapping. J. Opt. Soc. Am. A 13, 1999–2013.

Ghiglia, D.C., Pritt, M.D., 1998. Two-Dimensional Phase Unwrapping: Theory, Algorithms and Software, WileyBlackwell.

Goldstein, R.M., Zebker, H.A., Werner, C.L., 1988. Satellite radar interferometry: two-dimensional phase unwrapping. Radio Sci. 23 (4), 713–720.

Gourmelen, N., Amelung, F., Casu, F., Manzo, M., Lanari, R., 2007. Mining-related ground deformation in Crescent Valley, Nevada: implications for sparse GPS networks. Geophys. Res. Lett. 34 (9), L09, 309, <http://dx.doi.org/10.1029/2007GL029427>.

Gourmelen, N., Amelung, F., Lanari, R., 2010. Interferometric synthetic aperture radar–GPS integration: Interseismic strain accumulation across the Hunter mountain fault in the Eastern California shear zone. J. Geophys. Res. 115 (B9), 408.

Guneriussen, T., Hogda, K., Johnsen, H., Lauknes, I., 2002. InSAR for estimation of changes in snowwater equivalent of dry snow. Geosci. Remote Sens. IEEE Trans. 39 (10), 2101–2108.

Gutmann, B., Weber, H., 2000. Phase unwrapping with the branch-cut method: role of phase-field direction. Appl. Opt. 39 (26), 4802–4816.

Hanssen, R., Feijt A., 1997. A first quantitative evaluation of atmospheric effects on SAR interferometry, in ERS SAR Interferometry, vol. 406, p. 277.

Hanssen, R.F., 2001. Radar Interferometry: Data Interpretation and Error Analysis. Kluwer Academic, Dordrecht.

Hernández-Espriú, Antonio., Reyna-Gutiérrez, J.A., Sánchez-León, E., Cabral-Cano, E., Carrera-Hernández, J., Martínez-Santos, P., Macías-Medrano, S., Falorni, G., Colombo, D., 2014. The DRASTIC-Sg model: an extension to the DRASTIC approach for mapping groundwater vulnerability in aquifers subject to differential land subsidence, with application to Mexico City. Hydrogeol. J. 22, 1469–1485.

Herráez, M., Burton, D., Lalor, M., Gdeisat, M., 2002. Fast two-dimensional phase-unwrapping algorithm based on sorting by reliability following a noncontinuous path. Appl. Opt. 41 (35), 7437–7444.

Herrera, G., Notti, D., García-Davalillo, J.C., Mora, O., Cooksley, G., Sánchez, M., Crosetto, M., 2011. Analysis with C-and X-band satellite SAR data of the Portalet landslide area. Landslides 8 (2), 195–206.

Hong, S., Wdowinski, S., Kim, S., Won, J., 2010. Multi-temporal monitoring of wetland water levels in the Florida everglades using interferometric synthetic aperture radar (InSAR). Remote Sens. Environ. 114 (11), 2436–2447.

Hong, S.H., Wdowinski, S., 2014. Multitemporal multitrack monitoring of wetland Water levels in the Florida everglades using ALOS PALSAR data with interferometric processing. Geosci. Remote Sens. Lett. IEEE 11 (8), 1355–1359.

Hooper, A., Zebker, H., Segall, P., Kampes, B., 2004. A new method for measuring deformation on volcanoes and other natural terrains using InSAR persistent scatterers. Geophys. Res. Lett. 31 (23), 5.

Hooper, A., 2006. Persistent Scatter Radar Interferometry for Crustal Deformation Studies and Modeling of Volcanic Deformation, Ph.D. Thesis, Stanford University.

Hooper, A., Zebker, H.A., 2007. Phase unwrapping in three dimensions with application to InSAR time series. JOSA A 24 (9), 2737–2747.

Hooper, A., 2008. A multitemporal InSAR method incorporating both persistent scatterer and small baseline approaches. Geophys. Res. Lett. 35 (16).

Hooper, A., 2009. A Statistical-Cost Approach to Unwrapping the Phase of InSAR Time Series. In: Proceedings of ESA FRINGE Workshop, Frascati, Italy, November 30–December 4, 2009.

Hooper, A., Pedersen, R., Sigmundsson, F., 2009. Constraints on Magma Intrusion at Eyjafjallaj okull and Katla Volcanoes in Iceland, from Time Series SAR Interferometry, VOLUME Project, EU PF6, 18471, 978-1.

Hooper, A., 2010. A statistical-cost approach to unwrapping the phase of InSAR time series. In: Proceeding of International Workshop on ERS SAR Interferometry, vol. 30, Frascati, Italy.

Huntley, J.M., 2001. Three-dimensional noise-immune phase unwrapping algorithm. Appl. Opt. 40 (23), 3901–3908.

Itoh, K., 1982. Analysis of the phase unwrapping algorithm. Appl. Opt. 21 (14) (2470–2470).

Kampes, B.M., Hanssen, R.F., 2004. Ambiguity resolution for permanent scatterer interferometry. Geosci. Remote Sens. IEEE Trans. 42 (11), 2446–2453.

Kampes, B., 2005. Displacement Parameter Estimation using Permanent Scatterer Interferometry, Ph.D. Thesis, Technische Universiteit Delft.
Kampes, B., 2006. Radar Interferometry – Persistent Scatterer Technique, Remote Sensing and Digital Image Processing, vol. 12, Springer.
Karout, S., Gdeisat, M., Burton, D., Lalor, M., 2007. Residue vector, an approach to branch-cut placement in phase unwrapping: theoretical study. Appl. Opt. 46 (21), 4712–4727.
Kim, M., Griffiths, H., 1999. Phase unwrapping of multibaseline interferometry using Kalman filtering. IEE Conf. Publ. 1999 (CP465), 813–817. http://dx.doi.org/10.1049/cp:19990437.
Krämer, R. 1998. Auf Kalman-Filtern basierende phasen- und parameterestimation zur lösung der phasenvieldeutigkeitsproblematik bei der höhenmodellerstellung aus SAR-Interferogrammen, Ph.D. thesis, Universitat-GH Siegen.
Kuehn, F., Albiol, D., Cooksley, G., Duro, J., Granda, J., Haas, S., Hoffmann-Rothe, A., Murdohardono, D., 2010. Detection of land subsidence in Semarang, Indonesia, using stable points network (SPN) technique. Environ. Earth Sci. 60 (5), 909–992.
Lanari, R., Mora, O., Manunta, M., Mallorquí, J.J., Berardino, P., Sansosti, E., 2004. A small-baseline approach for investigating deformations on full-resolution differential SAR interferograms. Geosci. Remote Sens. IEEE Trans. 42 (7), 1377–1386.
Lanari, R., Casu, F., Manzo, M., Zeni, G., Berardino, P., Manunta, M., Pepe, A., 2007. An overview of the small baseline subset algorithm: a DInSAR technique for surface deformation analysis. Pure Appl. Geophys. 164 (4), 637–661.
Loffeld, O., Nies, H., Knedlik, S., Wang, Y., 2008. Phase unwrapping for SAR interferometry: a data fusion approach by Kalman filtering. Geosci. Remote Sens. IEEE Trans. 46 (1), 47–58. http://dx.doi.org/10.1109/TGRS.2007.909081.
Lu, Z., Dzurisin, D., 2014. Recent advances in InSAR image processing and analysis. In: InSAR Imaging of Aleutian Volcanoes. Springer, Berlin Heidelberg, pp. 35–48.
Luo, Q., Perissin, D., Dogan, O., Lin, H., Wang, W., 2012. Tianjin suburbs PS-QPS analysis and validation with leveling data. In Geoscience and Remote Sensing Symposium (IGARSS), 2012 IEEE International, pp. 3915–3918.
Martinez-Espla, J., Martinez-Marin, T., Lopez-Sanchez, J., 2009. A particle filter approach for InSAR phase filtering and unwrapping. IEEE Trans. Geosci. Remote Sens. 47 (4), 1197–1211.
Massonnet, D., Feigl, K., 1998. Radar interferometry and its application to changes in the earths surface. Rev. Geophys. 36 (4), 441–500.
Meyer, F., Nicoll J., 2009. The Impact of the ionosphere on interferometric SAR processing. In: Geoscience and Remote Sensing Symposium, 2008. IGARSS 2008. IEEE International, vol. 2, IEEE.
Miranda, N., Rosich, B., Santella, C., Grion M., 2003. Review of the impact of ERS-2 piloting modes on the SAR Doppler stability. In: Proc. FRINGE 2003 Workshop, Frascati. Italy, pp. 1–5.
Moisseev, D., Hanssen, R., Sabater J., 2005. Towards an atmosphere free interferogram; first comparison between ENVISAT's ASAR and MERIS water vapor observations. In: Geoscience and Remote Sensing Symposium, 2003. IGARSS'03. Proceedings. 2003 IEEE International, vol. 5, pp. 2977–2980.
Navarro, M.A., Estrada, J.C., Servin, M., Quiroga, J.A., Vargas, J., 2012. Fast two-dimensional simultaneous phase unwrapping and low-pass filtering. Opt. Express 20 (3), 2556–2561.
Nolan, M., Fatland, D., 2003. Penetration depth as a DInSAR observable and proxy for soil moisture. Geosci. Remote Sens. IEEE Trans. 41 (3), 532–537.
Nolan, M., Fatland, D., Hinzman, L., 2004. DInSAR measurement of soil moisture. Geosci. Remote Sens. IEEE Trans. 41 (12), 2802–2813.
Osmanoglu, B., Dixon, T.H., Wdowinski, S., Cabral-Cano, E., 2011a. On the importance of path for phase unwrapping in synthetic aperture radar interferometry. Appl. Opt. 50 (19), 3205–3220.
Osmanoglu, B., Dixon, T.H., Wdowinski, S., Cabral-Cano, E., Jiang, Y., 2011b. Mexico city subsidence observed with persistent scatterer InSAR. Int. J. Appl. Earth Obs. Geoinf. 13 (1), 1–12. http://dx.doi.org/10.1016/j.jag.2010. 05.009.
Parizzi, A., Brcic, R., 2011. Adaptive InSAR stack multilooking exploiting amplitude statistics: a comparison between different techniques and practical results. Geosci. Remote Sens. Lett. IEEE 99, 441–445.
Perissin, D., Ferretti, A., 2007. Urban-target recognition by means of repeated spaceborne SAR images. Geosci. Remote Sens. IEEE Trans. 45 (12), 4043–4058. http://dx.doi.org/10.1109/TGRS.2007.906092.
Perissin, D., Wang, T., 2012. Repeat-pass SAR interferometry with partially coherent targets. Geosci. Remote Sens. IEEE Trans. 50 (1), 271–280.
Pritt, M., Shipman, J., 1994. Least-squares two-dimensional phase unwrapping using FFT's. Geosci. Remote Sens. IEEE Trans. 32 (3), 706–708. http://dx.doi.org/10.1109/36.297989.
Rocca, F., Rucci, A., Ferretti, A., Bohane, A., 2013. Advanced InSAR interferometry for reservoir monitoring. First Break 31 (5).
Quiroga, J., Gonźalez-Cano, A., Bernabeu, E., 1995. Stable-marriages algorithm for preprocessing phase maps with discontinuity sources. Appl. Opt. 34 (23), 5029–5038.
Salfity, M.F., Ruiz, P.D., Huntley, J.M., Graves, M.J., Cusack, R., Beauregard, D.A., 2006. Branch cut surface placement for unwrapping of undersampled three-dimensional phase data: application to magnetic resonance imaging arterial flow mapping. Appl. Opt. 45 (12), 2711–2722.
Shanker, A.P., Zebker, H., 2010. Edgelist phase unwrapping algorithm for time series InSAR analysis. JOSA A 27 (3), 605–612.
Siles, G., Niemeier, W., Lopez-Quiroz, P., 2015. Interrelations between ground-water extraction, construction activities and ground subsidence in Valley of Mexico. In: GeoMonitoring Tagung 2015, pp. 93–104, ISBN: 3-938924-08-X.
Soergel, U. (Ed.), 2010. Radar Remote Sensing of Urban Areas, vol. 15. Springer Science & Business Media.
Sousa, J., Hooper, A., Hanssen, R., Bastos, L., 2009. Comparative study of two different PS-INSAR approaches: DEPSI vs. STAMPS. In: ESA Fringe Workshop 2009.
Tribolet, J., 1977. A new phase unwrapping algorithm. Acoustics. Speech Signal Process. IEEE Trans. 25 (2), 170–177.
Wegmuller, U., Werner, C., Strozzi, T., Wiesmann A., 2006. Ionospheric electron concentration effects on SAR and InSAR. In: Geoscience and Remote Sensing Symposium, 2006. IGARSS 2006. IEEE International Conference on, pp. 3731–3734, doi: http://dx.doi.org/10.1109/IGARSS.2006.956.
Werner, C., Wegmuller, U., Strozzi, T., Wiesmann, A., 2003. Interferometric point target analysis for deformation mapping. In: Geoscience and Remote Sensing Symposium, 2003. IGARSS'03. Proceedings. 2003 IEEE International, vol. 7, pp. 4362–4364.
Xu, W., Cumming, I., 1999. A region-growing algorithm for InSAR phase unwrapping. IEEE Trans. Geosci. Remote Sens. 37, 124–134. http://dx.doi.org/10.1109/36.739143.
Yan, Y., Lopez-Quiroz, P., Doin, M., Tupin, F., Fruneau, B., 2009. Comparison of two methods in multi-temporal differential SAR interferometry: application to the measurement of Mexico City subsidence. In: Fringe 2009, p. 8.
Yan, Y., Doin, M.P., López-Quiroz, P., Tupin, F., Fruneau, B., Pinel, V., Trouvé, E., 2012. Mexico City subsidence measured by InSAR time series: joint analysis using PS and SBAS approaches. Selected Top. Appl. Earth Observ. Remote Sens. IEEE J. 5 (4), 1312–1326.
Zebker, H.A., Villasenor, J., 1992. Decorrelation in interferometric radar echoes. IEEE Trans. Geosci. Remote Sens. 30, 950–959.
Zebker, H., Rosen, P., Hensley, S., 1997. Atmospheric effects in interferometric synthetic aperture radar surface deformation and topographic maps. J. Geophys. Res. 102 (B4), 7547–7563.
Zheng, D., Da, F., 2011. A novel algorithm for branch cut phase unwrapping. Opt. Lasers Eng. 49 (5), 609–617.